Signatures of tunneling and multiphoton ionization by short-laser pulses: The partial-wave distribution

2015 J. Phys.: Conf. Ser. 635 012003

(http://iopscience.iop.org/1742-6596/635/1/012003)

Journal of Physics: Conference Series **635** (2015) 012003 doi:10.1088/1742-6596/635/1/012003

Signatures of tunneling and multiphoton ionization by short-laser pulses: The partial-wave distribution

Diego G. Arbó [1], Christoph Lemell [2], and Joachim Burgdörfer [2]

[1] Institute for Astronomy and Space Physics, IAFE, CC 67, Suc. 28 (1428) Buenos Aires, Argentina

[2] Institute for Theoretical Physics, Vienna University of Technology, Wiedner Hauptstraße 8-10/136, A-1040 Vienna, Austria, EU

E-mail: diego@iafe.uba.ar

Abstract. We analyze the two-dimensional angular momentum-energy distribution of electrons emitted from argon by short laser pulses. We identify characteristic features of both multiphoton and tunneling ionization in the partial-wave distribution for Keldysh parameters close to unity. We observe a remarkable degree of quantum-classical correspondence in the photoinization process which becomes even more pronounced after intensity averaging over the focal volume. We derive an energy-dependent cut-off for the highest angular momentum accessible within the framework of the strong-field approximation, which accurately reproduces the partial wave distributions found from solutions of the time-dependent Schrödinger equation.

1. Introduction

Fully differential electron spectra emitted from atoms, molecules and condensed matter by ultrashort strong few-cycle laser pulses have become available very recently [1, 2]. Extending the investigation from near-infrared (NIR, with $\lambda = 800$ nm) to mid-infrared fields (MIR, with $\lambda = 2$ to 4 μm) yielded unexpected structures at very low energies ("ionization surprises" [3, 4]). Also for NIR, fully two-dimensional momentum maps [1, 2] displayed complex patterns featuring signatures of both multiphoton and tunneling ionization. While at high momenta remnants of above threshold ionization (ATI) peaks are visible which are a characteristic of multiphoton ionization, near threshold a pattern of angular nodes appears in the doubly-differential momentum distribution which has been both experimentally observed and theoretically analyzed [5, 6, 7, 8, 9, 10]. The origin of near-threshold structures was related [6] to the dominance of a single partial wave l_0 giving rise to an angular nodal pattern according to the Legendre polynomial $\sim [P_{l_0}(\cos\theta)]^2$. Semiclassically, a multitude of paths reach the same emission angle having nearly the same angular momentum and leads to an interference pattern in complete analogy to generalized Ramsauer-Townsend (GRT) diffraction oscillations in electron - atom (or ion) scattering [6]. The fact that the near-threshold angular distribution could be alternatively explained in terms of interferences among paths or by the deep quantum limit of a single quantum number raised conceptual questions as to the underlying quantum-classical correspondence. Recently, the study of classical-quantum correspondence was extended to MIR pulses deep into the tunneling regime showing multiple peak and interference structures into the electron energy-angular momentum plane [11].

In the present communication we explore the partial-wave distribution in the continuum or, classically, the two dimensional distribution in the energy (E) and angular momentum (L) plane for strong-field ionization of argon by few-cycle NIR pulses in the transition regime between tunneling (Keldysh parameters $\gamma < 1$) and multiphoton ionization ($\gamma > 1$), see Ref. [12]. While the two-dimensional $E - L$ distribution is, unlike the vectorial linear momentum $(p_{\parallel}, p_{\perp})$ distributions (parallel and perpendicular to the laser polarization) in general not directly observable, it nevertheless controls the multi-differential electron distribution and can provide novel insights in the ionization process. We present results of doubly differential angular momentum and energy distributions of emitted electrons by solving the time-dependent Schrödinger equation (TDSE) and performing classical-trajectory Monte-Carlo (CTMC) calculations. We explore the connection between the classical and the quantum dynamics by providing an analytic approximation of the maximum angular momentum acquired for a given (near threshold) energy. This model combines the description of tunneling ionization within the strong-field approximation (SFA) with the asymptotic propagation on perturbed Coulomb trajectories.

The present article is organized as follows. In Sec. 2, we briefly review the theoretical models employed. In Sec. 3 we present an analytical semiclassical prediction for the cut-off angular momentum L_c reached in tunneling ionization. A detailed comparison between classical and quantum calculations with the semiclassical prediction is presented in Sec. 4 followed by conclusions in Sec. 5. Atomic units are used throughout unless stated elsewise.

2. Theoretical models

2.1. Solution of the time-dependent Schrödinger equation

The Hamiltonian of an atom interacting with a laser field within the single active electron approximation (SAE) and in the length gauge reads

$$H = \frac{\vec{p}^2}{2} + V(r) + \vec{r} \cdot \vec{F}\,(t), \tag{1}$$

where $\vec{p}$ and $\vec{r}$ are the momentum and position of the electron, respectively, $V(r)$ is the atomic central potential, and $\vec{F}(t)$ is the time dependent external field. The linearly polarized laser field is chosen to be of the form

$$\vec{F}(t) = F_0 \sin^2\left(\frac{\pi t}{\tau}\right) \cos(\omega t)\hat{z};\ 0 \le t \le \tau\ , \tag{2}$$

and zero elsewhere. In Eq. (2), ω is the laser carrier frequency, τ is the total pulse duration, F_0 the peak field, and $\hat{z}$ is the polarization direction. The carrier-envelope phase was chosen to be zero so that we deal with cosine-like pulses. We employ for $V(r)$ a model potential with an asymptotic Coulomb tail ($\sim -1/r$) and a short-range potential accounting for the influence of the ionic core of Ar^+ reproducing the correct ionization potential $I_p = 15.76$ eV (0.58 a.u.) and the energies of low-lying excited bound states [13].

We solve the TDSE employing the generalized pseudo-spectral method [14, 15, 16]. This method combines the discretization of the radial coordinate optimized for the Coulomb singularity with quadrature methods to allow stable long-time evolution using a split-operator method. Both the unbound as well as the bound parts of the wave function $|\psi(t)\rangle$ can be accurately represented. Propagation of the wavefunction starts from the initial $3p$ ground state orbitals φ_{3p0} since the ionization from the $m = 0$ orbital, aligned along the laser polarization axis, strongly dominates over $m = -1, 1$ in the resulting spectrum. Due to the cylindrical symmetry of the atom in a linearly polarized laser field, the magnetic quantum number is conserved during the time evolution. Once the pulse is over, the wavefunction is projected onto eigenstates $|k, l\rangle$ of the field-free atomic Hamiltonian with positive eigenenergy $E = k^2/2$ and orbital quantum number l in order to determine the transition amplitudes $t_{i\to kl}$.

2.2. Classical-trajectory Monte-Carlo method

Our classical-trajectory Monte-Carlo simulation has been described in detail elsewhere [17]. Briefly, using the ADK tunneling rates for electrons [18] the distribution of starting times t_0 for the propagation of classical trajectories following Newton's equation of motion is determined. The initial conditions for the longitudinal and perpendicular momenta at the tunnel exit are taken from Ref. [19]. The trajectory of emitted electrons in the combined laser and ionic fields is calculated using a standard fourth-order Runge-Kutta solver. The final $E-L$ distribution is extracted by relating the outgoing trajectory onto Kepler hyperbolas for a given E and L. For mapping the classical angular momentum L to the partial-wave quantum number we use the Langer connection $L = l + 1/2$ which corresponds to the binning of continuously distributed L according to $l \leq L \leq l + 1/2$.

3. Semiclassical models for the partial-wave distributions

3.1. Tunneling ionization

Within the semiclassical approximation to strong-field ionization in the tunneling regime, atomic ionization proceeds by tunneling through the barrier formed by the atomic potential and the interaction with the electric field, followed by the propagation in the oscillating electric field [20]. In the following, we derive an analytic estimate for the cut-off angular momentum $L_c(E)$ for this scenario that treats the tunneling ionization step within the SFA but approximately includes the effect of the asymptotic Coulomb field by linking the tunnel ionization with the motion on Kepler hyperbolae.

The starting point is the SFA, which we evaluate in the semiclassical limit, the saddle-point approximation (SPA). It describes ionization in terms of quantum trajectories emerging from the tunnel barrier that start at complex ionization times t_r. They are given by the solutions of the equation [21, 22, 23, 24, 25, 26]

$$\frac{\left[\vec{k} + \vec{A}(t_r)\right]^2}{2} + I_p = 0, \tag{3}$$

where I_p is the ionization potential of the atom, $\vec{A}(t) = -\int_0^t dt' \vec{F}(t')$ is the vector potential multiplied by the speed of light, and $\vec{k}$ is the final momentum of the escaping electron. In the following analytic treatment we neglect for simplicity variations of the envelope of the field, implying a continuum wave (cw), while the TDSE and CTMC calculations fully account for the envelope function of the few-cycle pulse. Eq. (3) has a pair of complex solutions per optical cycle j, $t_{1j} = \frac{1}{\omega}\sin^{-1}[\tilde{\kappa}] + \frac{2\pi}{\omega}(j-1)$, and $t_{2j} = \frac{-1}{\omega}\sin^{-1}[\tilde{\kappa}^*] + \frac{2\pi}{\omega}(j-\frac{1}{2})$, where $\tilde{\kappa}$ denotes the scaled complex final momentum defined by $\tilde{\kappa} = \kappa_z + i\sqrt{\kappa_\rho^2 + \gamma^2}$, κ_z and κ_ρ are the cylindrical components (parallel and perpendicular to the polarization direction $\hat{z}$) of the dimensionless final momentum of the electron $\vec{\kappa} = \omega\vec{k}/F_0$, and $\gamma = \sqrt{2I_p}\omega/F_0$ is the Keldysh parameter.

We analyze the semiclassical equations of motion within the SPA for the first saddle point $t_1 \equiv t_{11} = \frac{i}{\omega}\sinh^{-1}[\gamma]$ for electron emission near threshold by setting $k_z = k_\rho = 0$. Solving Newton's equations of motion on the imaginary time axis between $t = t_1$ and $t = 0$ (see Fig. 1a inset) subject to the mixed boundary conditions that the electron takes off at the nucleus ($z(t_1) = 0$) and arrives at the tunneling exit $z(0)$ at $t = 0$ with zero velocity ($\dot{z}(0) = 0$) yields to the time-dependent projection of the electron position along the polarization axis (Fig. 1a)

$$z(t) = \alpha\left[\sqrt{1+\gamma^2} - \cos(\omega t)\right], \tag{4}$$

where $\alpha = F_0/\omega^2$ is the amplitude of the quiver oscillation. Accordingly, the z coordinate at the tunneling exit is given by

$$z(0) = \alpha\left(\sqrt{1+\gamma^2} - 1\right). \tag{5}$$

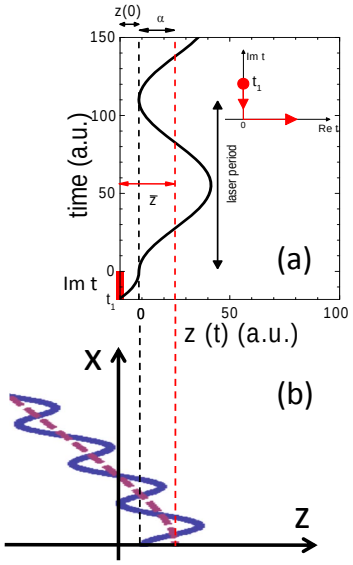

Figure 1. (color online): (a) Semiclassical electron position (with zero final kinetic energy) corresponding to the passage of the electron through the potential barrier from $t = t_1$ to $t = 0$ followed by the electron oscillation driven by the electric field ($\omega = 0.057$, $F_0 = 0.08$, $I = 2.25 \times 10^{14}$ W/cm^2, $I_p = 0.58$). Inset shows the integration path in the time complex plane. (b) Schematic electron trajectory showing the oscillation with quiver amplitude α around a Kepler hyperbola with final momentum $\vec{k} \neq 0$.

Equations (4) and (5) apply to short (or zero) ranged binding potentials i.e., the Coulomb potential forming an extended atomic potential well is neglected. Tunneling starts at $z(t_1)$ and after emerging at the tunneling exit at $t = 0$, the electron undergoes quiver oscillations with amplitude α about the center coordinate (Fig. 1)

$$\begin{aligned} \bar{z} &= z(0) + \alpha \\ &= \alpha\sqrt{1+\gamma^2}. \end{aligned} \tag{6}$$

In the deep tunneling limit ($\gamma \to 0$), the position of the tunneling exit [Eq. (5)] becomes

$$z(0) = \alpha\gamma^2/2 = I_p/F_0, \tag{7}$$

and the center coordinate for the quiver oscillation

$$\bar{z} = \alpha\left(1 + \frac{\gamma^2}{2}\right). \tag{8}$$

Conversely, in the multiphoton limit ($\gamma \to \infty$), the center coordinate

$$\bar{z} \simeq \alpha\gamma = \sqrt{2I_p}/\omega \tag{9}$$

becomes independent of the laser intensity. The physical significance of this limit [Eq. (9)] is, however, not obvious as it is derived from a semiclassical tunneling approach.

We link now the strong-field tunneling dynamics at small distances with the propagation in the asymptotic Coulomb field by surmising that the quiver oscillation is superimposed on a drift motion following a Kepler hyperbola with the same final momentum (see Fig. 1b) [6, 7]. Short-range deviations from the asymptotic Coulomb potential can be neglected for distances from the nucleus larger than the tunneling exit $z(0)$. Semiclassically, the electron trajectories released at different times reaching the same asymptotic branch of the Kepler hyperbola interfere: the number of quiver oscillations along the Kepler orbit reaching the same asymptote is not unique thus allowing for path interferences leading to the "bouquet"-shape structure in the doubly differential momentum distribution [6, 7]. The link is made quantitative by identifying the center coordinate $\bar{z}$ after tunneling with the pericenter $r_{\min}$ of the outgoing Kepler hyperbola in

the Coulomb field. As the distance of the electron at the tunneling exit cannot be larger than $z(0)$ in Eq. (5), then $r_{\min} \leq \bar{z}$. This provides an upper cut-off to the angular momentum for a given final energy of the Kepler orbit, $L \leq L_c(E)$, where

$$L_c(E) = \left[2Z_T\bar{z}(1+\frac{\bar{z}E}{Z_T})\right]^{1/2} \tag{10}$$

with Z_T the asymptotic charge of the atomic potential, i.e., $V(r) \to -Z_T/r$ as $r \to \infty$ [27]. Eq. (10) applies to small kinetic energies, as $\bar{z}$ was calculated for electrons with zero kinetic energy. Considering electrons with zero final kinetic energy (at threshold), Eq. (10) becomes

$$L_c = L_c(0) = \left(2Z_T\alpha\sqrt{1+\gamma^2}\right)^{1/2}. \tag{11}$$

For zero Keldysh parameter $\gamma = 0$, $\bar{z} = \alpha$ the Simple Man's Model (SMM) [28] version of Eq. (11) $L_c^{\rm SMM} = (2Z_T\alpha)^{1/2}$ emerges in agreement with the semiclassical estimate given in Ref. [6]. There, however, $L_c^{\rm SMM}$ was taken as estimate for the dominant angular momentum for near-threshold electrons. The present analysis suggests that Eq. (10) provides an upper limit for (semi-)classically allowed electron angular momenta, hence, partial wave l, irrespective of the atomic species provided that the long range Coulomb force dominates. In Fig. 2, we illustrate the predictions $L_c(E)$ and $L_c^{\rm SMM}(E)$ for a laser frequency $\omega = 0.057$ ($\lambda = 800$ nm) and electric field $F_0 = 0.0533$ ($I = 10^{14}$ W/cm^2). We observe that always $L_c^{\rm SMM}(E) < L_c(E)$. The implication of Eq. (10) is that the partial wave probability $p_l(E)$ is small for $l > L_c(E)$.

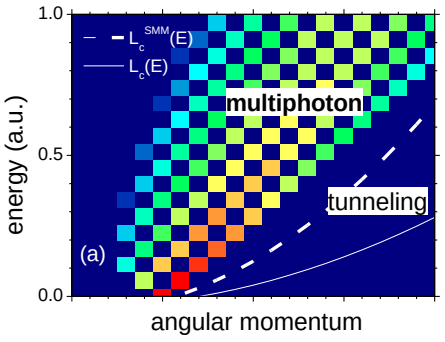

Figure 2. (color online): (color online): Schematic representation of multiphoton and tunneling contribution to argon ionization by a laser pulse as a function of energy and angular momentum of the ejected electron. Dashed line and solid line correspond to $L_c^{\rm SMM}(E)$ and $L_c(E)$, respectively.

3.2. Multiphoton ionization

For the multiphoton regime ($\gamma \gg 1$), the partial wave distribution in the continuum, $p_l(E)$ can be modelled in terms of a biassed random walk in $E-l$ space [6, 29, 9]. Each photoabsorption event is viewed as a discrete jump between points in the $E-l$ plane $(E_n, l_n) \to (E_{n+1} = E_n + \omega, l_{n+1} = l_n \pm 1)$ with the energies corrected for the ponderomotive shift, $E = n\omega - I_p - U_p$, where $U_p = (F_0/2\omega)^2 \propto I/\omega$ is the ponderomotive energy and n is the number of absorbed photons [9]. Assuming a stochastic uncorrelated multi-photon process, the partial wave populations $p_l(E)$, $(l = 0, 1, 2, ...)$ are the result of a sequence of a large number of random angular momentum changing photoabsorption processes [9]. The electron with orbital quantum number l can absorb a photon and consequently undergoes a transition $l \to l+1$ with a probability p_+ or a transition $l \to l-1$ with a probability p_-, according to the dipole coupling and the selection rule $\Delta l = \pm 1$. As photon-absorption has a propensity of populating higher angular momentum states, $p_+ > p_-$, the random walk is biassed. Starting from the argon $3p$ state, the random walk reaches even parity states when n is odd and odd parity states when n is even. At a fixed energy E_n in

the continuum, either only even or only odd $p_l(E_n)$ are populated. Fig. 2 illustrates a typical partial-wave distribution in the continuum assuming that at threshold $l_0 = 5$, and $p_+ = 0.8$ and $p_- = 0.2$ (see [6]). The qualitative picture remains unchanged for different choices of p_+ and p_-, as long as $p_+ > p_-$.

One characteristic feature is that the partial wave populations are suppressed for l beyond the line $E(L) = \omega(L - l_0)$ corresponding to $\Delta l = +1$ transitions. On the other hand, the border line $E(L) = -\omega(L - l_0)$ corresponding to $\Delta l = -1$ is not clearly observed because of the strongly asymmetric values of p_+ and p_- used. This random walk picture is obviously an oversimplification of the multiphotoionization process, yet can still explain qualitative features seen in the full TDSE solution.

4. Comparison between TDSE and semiclassical models

We analyze now the partial-wave populations, $p_l(E) = |\langle k, l|\psi(\tau)\rangle|^2$, extracted from the solution of the TDSE in the light of the classical and semiclassical models. The TDSE distribution for an ultrashort pulse with laser frequency $\omega = 0.057$, peak electric field $F_0 = 0.053$ ($I = 10^{14}$ W/cm^2 and $\gamma = 1.15$), and total pulse duration $\tau = 882$ (21 fs, 8.2 fs FWHM intensity) corresponding to eight full optical cycles (Fig. 3a) is remarkably well confined by the border line $L_c(E)$ [Eq. (10)] derived from the semiclassical tunnel ionization model. For a better comparison to classical calculations, the angular momentum is plotted as a continuum variable, despite its discrete nature in quantum mechanics. In order to do so, we smooth the distribution in the L component with a window function of width of the same order of the quantum discretization $/DeltaL = 1$. Horizontal iso-energy stripes separated by the photon energy are a clear signature of multiphoton absorption. In addition, we observe a broad structure starting at threshold from $l_0 \sim 0$ to $l_0 \sim 7$ and extending diagonally with slope ω, in agreement with multiphoton absorption with $\Delta l = 1$. For example, several maxima of the distribution lie on the dotted line $\Delta L = 1$ and other maxima follow straight lines parallel to the dotted line in Fig. 3a. Neighboring local maxima into this diagonal structure are horizontally separated by a spacing $\Delta l = 2$ reflecting the selection rule $\Delta l = \pm 1$ characteristic of the multiphoton absorption. As expected, both tunneling and multiphoton features coexist in Fig. 3 (a) with the Keldysh parameter $\gamma = 1.15$, in the transition between the tunneling and multiphoton regimes.

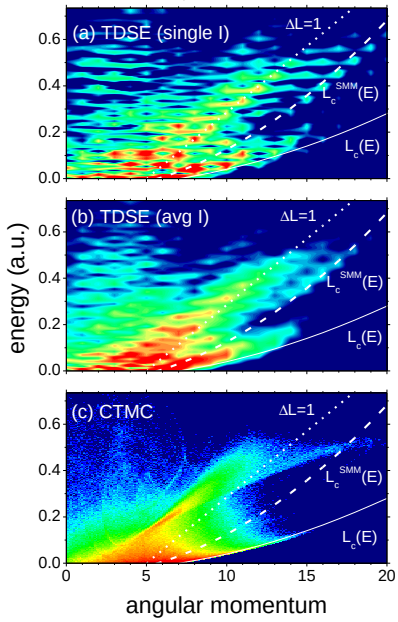

Figure 3. (color online): Electron yield after argon ionization as a function of the energy and angular momentum in logarithmic scale covering two orders of magnitude. Dotted line corresponds to multiphoton $E(L) = \omega(L - l_0)$ contribution with $l_0 = 5$, dashed line corresponds to $L_c^{\rm SMM}(E)$, and solid line corresponds to $L_c(E)$. (a) TDSE without averaging over the focal volume, (b) TDSE averaging over the focal volume, and (c) CTMC. The parameters of the laser field are: $\omega = 0.057$, $\tau = 882$, and $F_0 = 0.0533$ ($I = 10^{14}$ W/cm^2).

For a more detailed comparison between quantum and classical calculations, we have performed an intensity average over the focal volume of the laser pulse [30]. Assuming a cylindrically symmetric beam with Gaussian intensity profile and maximum intensity I_0, the volume with intensities larger than I_i is given by

$$V(I > I_i) \propto 2\beta + \beta^3/3 - 2\arctan\beta \tag{12}$$

with $\beta = \sqrt{I_0/I_i - 1}$. In order to perform the intensity averaged partial-wave photoelectron distribution shown in Fig. 3b we have performed TDSE calculations for twenty one different intensities ranging from a maximum value of intensity $I = 10^{14}$ W/cm^2 to a minimum value $I/4$ (below this minimum value, ionization is negligible). As compared to single intensity calculations (Fig. 3a), the fringe visibility of the ATI horizontal stripes is reduced after averaging, though signatures of both tunneling and multiphoton absorption are still evident. A finger-shape structure between the SMM and SPA predictions [Eq. (10)] of tunneling ionization can be seen. The broad stripe with slope ω characteristic for multiphoton absorption can be still observed after intensity averaging.

We have also simulated the ionization of argon within the CTMC method. As for the solution of the TDSE, we have performed an intensity average over the focal intensity distribution [Eq. (12)]. As expected, the distribution in Fig. 3c lacks signatures of interference e.g., the ATI iso-energy horizontal stripe observed in quantum calculations. However, the resemblance between classical (Fig. 3c) and quantum distributions (Fig. 3b) is remarkable exhibiting a high degree of quantum-classical correspondence. Even the diagonal structure is present, although slightly displaced and with smaller slope. The origin of this appearance and shape in a CTMC simulation is subject to further studies. It is worth noting that the SPA angular momentum cut-off $L_c(E)$ [Eq. (10)] closely agrees with the border of the classical energy-angular momentum distribution (Fig. 3c). This remarkable agreement strongly supports the linking of the coordinate of the tunneling exit $z(0)$ to the classical Kepler orbit used in Eq. (10) via the center coordinate $\bar{z}$ [Eq. (6)] (see Fig. 1).

In order to analyze the near-threshold ionization in more detail, we determine the integrated partial wave probabilities p_l contributing to the first ATI peak, i.e., up to the first minimum in the energy Λ [6],

$$p_l = \int_0^{\Lambda} dE\ p_l(E) = \int_0^{\sqrt{2\Lambda}} k dk |\langle k, l|\psi(\tau)\rangle|^2 \,. \tag{13}$$

The value of Λ can either be obtained graphically from the photoelectron spectrum or numerically from the midpoint energy between first and second ATI in the continuum, i.e., $\Lambda = (E_n + E_{n+1})/2$, where $E_n = n\omega - I_p - U_p$. In the present case with $\Lambda \simeq 0.02$ a.u., the normalized partial population $p_l/\sum_l p_l$ (Fig. 4) for a range of intensities varying from $I = 3.2 \times 10^{13}$ W/cm^2 ($F_0 = 0.03$) to $I = 2.25 \times 10^{14}$ W/cm^2 ($F_0 = 0.08$) appears irregularly fluctuating prior to intensity averaging (Fig. 4a) while conforming to the cut-off limit $L_c(E)$. Only after intensity averaging (Fig. 4b), a smoother distribution with a dominant partial wave emerges for $F_0 \gtrsim 0.04$. We also include the predicted values of L_c and $L_c^{\rm SMM}$ [Eq. (11)]. Both predictions approach each other as the peak electric field F_0 increases ($\gamma \to 0$) and reproduce the dominant angular momentum very well. Furthermore, CTMC reproduces the intensity averaged TDSE near threshold partial waves p_l very well, especially at high electric fields (low Keldysh parameters).

Finally, we have also calculated the average angular momentum $\langle l\rangle = \sum_l l\ p_l/\sum_l p_l$ near threshold ($E < \Lambda$) for a broad range of laser intensities (Fig. 5). Prior to averaging over the focal volume the TDSE results display irregular fluctuations as a function of the intensity. After intensity averaging, $\langle l\rangle$ display a smooth overall increasing behavior as laser intensity increases.

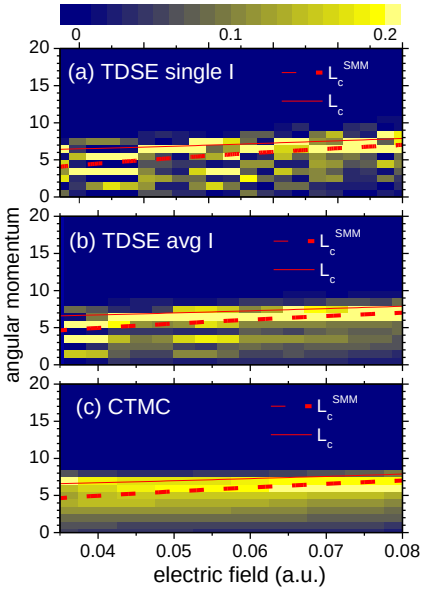

Figure 4. (color online): Normalized populations $p_l/\sum_l p_l$ near threshold ($E < 0.02$) for a range of laser peak fields in linear scale. The parameters of the laser field are: $\omega = 0.057$, $\tau = 882$, as a function of F_0. Dashed line and solid line correspond to SMM and SPA predictions [Eq. (11)], respectively. TDSE without (a) and with (b) averaging over the focal volume, and CTMC (c).

CTMC results reproduce the intensity averaged TDSE near-threshold $\langle l \rangle$. The SMM relation $L_c^{\rm SMM}$ provides a remarkably good estimate for the average angular momentum at threshold. As expected, $\langle l \rangle$ lies for all intensities well below the cut-off value L_c.

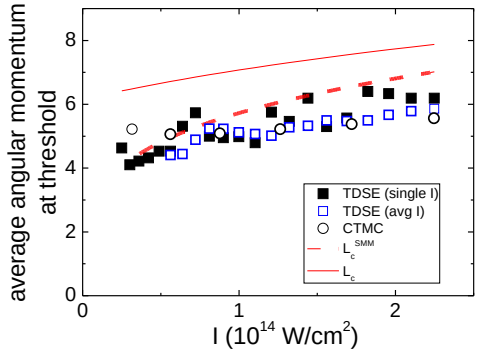

Figure 5. (color online): Mean value of the angular momentum $\langle l \rangle$ near threshold as a function of the intensity of the laser. Calculations within the TDSE with (open squares) and without (full squares) averaging over the focal volume, and CTMC (open circles). Dashed line and solid line correspond to SMM and SPA predictions [Eq. (11)], respectively.

5. Conclusions

Photoionization of argon by few-cycle laser pulses exhibits both multiphoton and tunneling features for intermediate values between the Keldysh parameters ($\gamma \sim 1$). We find a remarkable resemblance of CTMC and TDSE doubly-differential energy-angular momentum distributions after averaging over the focal volume. Thus, the photoionization process exhibits a high degree of classical-quantum correspondence especially in the tunneling regime for smaller Keldysh parameters. We have observed that the doubly-differential $E - L$ distribution is limited by the cut-off estimate $L_c(E)$ [Eq. (10)]. The latter has been shown to be the energy-dependent maximum angular momentum the electron can acquire on a Kepler orbit with the pericenter coinciding with the center coordinate of the quiver oscillation after tunneling ionization. The current analysis of the cut-off estimate for the direct electron emission helps to determine the rescattering nature of the multiple peak structures near threshold in [17, 11, 32, 4] at the time of analyzing the classical-quantum correspondence in atomic ionization by midinfrared pulses (see

[11]), especially the low-energy structures found in [4]. The pericenter of the Kepler hyperbola can be semiclassically estimated from the sum of the distance of the tunnel exit and the quiver amplitude α. We find that the dominant angular momentum near threshold depends only weakly on the laser intensity.

Acknowledgments
Work supported by CONICET PIP0386, Austria-Argentina collaboration AU/12/02 and PICT2010-1084 of ANPCyT (Argentina), the University of Buenos Aires (UBACyT617), by the FWF special research programs SFB-041 (ViCoM) and SFB-049 (NextLite), doctoral programme DK-W1243 (Solid4Fun), FWF project P21141-N16, by the European COST Action CM1204 (XLIC) and a WTZ project of the OeAD (AR 03/2013).

References

[1] Maharjan C M, Alnaser A S, Litvinyuk I, Ranitovic P and Cocke C L 2006 *J. Phys. B* **39** 1955
[2] Rudenko A, Zrost K, Schröter C D, de Jesus V L B, Feuerstein B, Moshammer R and Ullrich J 2004 *J. Phys. B* **37**, L407-L413
[3] Faisal F H M 2009, *Nat. Phys.* **5** 319
[4] Blaga C I, Catoire F, Colosimo P, Paulus G G, Muller H G, Agostini P and DiMauro L F 2009 *Nature Phys.* **5** 335
[5] de Bohan A 2001 *Ph.D. thesis*, Université Catholique de Louvain
[6] Arbó D G, Yoshida S, Persson E, Dimitriou K I and Burgdörfer J. 2006 *Phys. Rev. Lett.* **96** 143003
[7] Arbó D G, Dimitriou K I, Persson E and Burgdörfer J 2008 *Phys. Rev. A* **78** 013406
[8] Arbó D G, Miraglia J E, Gravielle M S, Schiessl K, Persson E and Burgdörfer J 2008 *Phys. Rev. A* **77** 013401
[9] Chen Z, Morishita T, Le A-T, Wickenhauser M, Tong X M and Lin C D 2006 *Phys. Rev. A* **74** 053405
[10] Wickenhauser M, Tong X M, Arbó D G, Burgdörfer J and Lin C D2006 *Phys. Rev. A* **74** 041402(R)
[11] Lemell C, Burgdörfer J, Gräfe S, Dimitriou K I, Arbó D G and Tong X-M 2013 *Phys. Rev. A* **87** 013421
[12] V. Keldysh 1964, Zh. Eksp. Theo. Fiz. **47**, 1945; 1965 Sov. Phys. JETP **20**, 1307
[13] Muller H G, Bucksbaum P H, Schumacher D W and Zavriyev A 1990 *J. Phys. B* **23** 2761
[14] Tong X-M and Chu S I 1997 *Chem. Phys.* **217** 119
[15] Tong X-M and Chu Shih-I 2000 *Phys. Rev. A* **61** 031401(R)
[16] Tong X-M and Lin C D 2005 *J. Phys. B* **38** 2593
[17] Wolter B *et al.* 2014 *Phys. Rev. A* **90** 063424
[18] Ammosov M V, Delone N B and Krainov V P 1986 *Zh. Eksp. Teor. Fiz.* **91**, 2008;1986 *Sov. Phys. JETP* **64** 1191
[19] Delone N B and Krainov V P 1991 *J. Opt. Soc. Am. B* **8** 1207
[20] Perelemov A M, Popov V S and Terent'ev M V 1967 *Soviet Physics JETP* **24** 207
[21] Arbó D G, Nagele S, Tong X-M, Xie X, Kitzler M and Burgdörfer J 2014 *Phys. Rev. A* **89** 043414
[22] Arbó D G, Ishikawa K L, Schiessl K, Persson E and Burgdörfer J 2010 *Phys. Rev. A* **81** 021403(R)
[23] Arbó D G, Ishikawa K L, Schiessl K, Persson E and Burgdörfer J 2010 *Phys. Rev. A* **82** 043426
[24] Milošević D B, Hasović E, Odžak S, Busuladžić M, Gazibegović-Busuladžić A and Becker W 2008 *J. Mod. Opt.* **55** 2653
[25] Milošević D B and Becker W 2002 *Phys. Rev. A* **66** 063417
[26] Milošević D B, Hasovic E, Busuladzic M, Gazibegovic-Busuladzic A and Becker W 2007 *Phys. Rev. A* **76** 053410
[27] Landau L D and Lifshitz E M 1960 *Mechanics* (Pergamon Press, Oxford)
[28] van Linden van den Heuvell H B and Muller H G 1988 *Multiphoton Processes (*ed. S.J. Smith and P.L. Knight, Cambridge University Press)
[29] Morishita T, Chen Z, Watanabe S and Lin C D 2007 *Phys. Rev. A* **75** 023407
[30] Augst S, Meyerhofer D D, Strickland and Chin S L 1991 *J. Opt. Soc. Am. B* **8** 858
[31] Langer R E 1937 *Phys. Rev.* **51** 669
[32] Lemell C, Dimitriou K I, Tong X-M, Nagele S, Kartashov D, Burgdörfer J and Gräfe S 2012 *Phys. Rev. A* **85** 01403(R)